MATERIALS SCIENCE

Smart contact lens and transparent heat patch for remote monitoring and therapy of chronic ocular surface inflammation using mobiles

Jiuk Jang[1,2]*, Joohee Kim[1,2]*, Haein Shin[1,2], Young-Geun Park[1,2,3], Byung Jun Joo[1,2], Hunkyu Seo[1,2], Jong-eun Won[2,4,5], Dai Woo Kim[6,7], Chang Young Lee[8], Hong Kyun Kim[6,7]†, Jang-Ung Park[1,2,3]†

Wearable electronic devices that can monitor physiological signals of the human body to provide biomedical information have been drawing extensive interests for sustainable personal health management. Here, we report a human pilot trial of a soft, smart contact lens and a skin-attachable therapeutic device for wireless monitoring and therapy of chronic ocular surface inflammation (OSI). As a diagnostic device, this smart contact lens enables real-time measurement of the concentration of matrix metalloproteinase-9, a biomarker for OSI, in tears using a graphene field-effect transistor. As a therapeutic device, we also fabricated a stretchable and transparent heat patch attachable on the human eyelid conformably. Both diagnostic and therapeutic devices can be incorporated using a smartphone for their wireless communications, thereby achieving instantaneous diagnosis of OSI and automated hyperthermia treatments. Furthermore, in vivo tests using live animals and human subjects confirm their good biocompatibility and reliability as a noninvasive, mobile health care solution.

INTRODUCTION

Wearable electronic devices with deformable structures that can monitor biomedical information of the human body wirelessly have been extensively explored over the past decade as a key for next-generation electronics (1–11). They aim to realize a personal health care system by measuring biomarkers in various biological interfaces, including skin (1, 2), ocular surfaces (12–16), and mouths (17). Sweat and tears can be especially attractive for the clinical diagnosis of chronic diseases (e.g., diabetes, chronic kidney syndrome, and pulmonary diseases) because they can be monitored noninvasively and consistently using these wearable devices (18). Among these diseases, the diagnosis and treatment of chronic ocular surface inflammatory disease, including dry eye syndrome (DES) and meibomian gland dysfunction (MGD), are of emerging interest because their prevalence is steadily increasing in the general population. It is related to the increasing daily screen time of people, air pollution, and aging society (19). Currently, chronic ocular surface inflammation (OSI) can be diagnosed by several tests, including epithelial abnormalities, tear film test, the degree of conjunctival injection, and questionnaires for evaluating the severity of subjective symptoms (table S1). Some diagnostic criteria have been proposed using these conventional diagnostic methods (20). However, substantial

numbers of patients reporting symptoms of chronic OSI can be negative with conventional criteria. Furthermore, none of the tests are available for screening, predicting the prognosis and showing responsiveness to treatment (19, 21). Matrix metalloproteinase-9 (MMP-9), which is an essential endopeptidase for pathological analyses, has been used as a biomarker for diagnosing chronic OSI because it is correlated tightly with the inflammatory status of ocular surfaces. Although a qualitative test with MMP-9 has been available, this test cannot quantify and digitize the degree of chronic OSI (19, 22, 23). Therefore, wearable smart sensors that can monitor OSI quantitatively in real time are highly desirable for use in mobile health care. In addition to this diagnosis, acute and consistent therapy is also important due to the difficulty in curing chronic OSI completely after the symptoms become apparent. Several medical devices, such as the Lipiflow thermal pulsation device (TearScience, Morrisville, NC, USA) that maintains the treatment temperature to the eyelids or the treatment using intense pulse light (IPL), were recently introduced for the effective treatment of OSI. However, these devices and methods can only be applied in clinics and cannot be used in daily life because they are relatively bulky and obstruct the user's vision. (20, 24, 25).

Here, we report an integrated system for real-time, remote monitoring and therapy for chronic OSI. This system consists of both a soft, smart contact lens for the diagnosis and an eyelid-attachable heat patch for hyperthermia treatment. Our development of this point-of-care system involves several unique strategies as follows. First, as a diagnostic device, we fabricated a smart, soft contact lens that enables remote and quantitative analysis of the MMP-9 level in the wearer's tears using mobile phones. A graphene field-effect transistor (FET) biosensor that can detect the concentration of MMP-9 in tear fluids, as a protein biomarker of OSI (22, 26), is integrated with a wireless antenna, capacitors, resistors, and a near-field communication (NFC) chip through stretchable interconnects to compose this smart contact lens without obstructing the wearer's view. This contact lens enables the real-time wireless transmission

[1]Nano Science Technology Institute, Department of Materials Science and Engineering, Yonsei University, Seoul 03722, Republic of Korea. [2]Center for Nanomedicine, Institute for Basic Science (IBS), Seoul 03722, Republic of Korea. [3]KIURI Institute, Yonsei University, Seoul 03722, Republic of Korea. [4]Department of Dentistry, Korea University Guro Hospital, Seoul 08308, Republic of Korea. [5]Institute of Clinical Dental Research, Korea University Guro Hospital, Seoul 08308, Republic of Korea. [6]Department of Ophthalmology, School of Medicine, Kyungpook National University, 680 Gukchaebosang-ro, Jung-gu, Daegu 41944, South Korea. [7]Bio-Medical Institute, Kyungpook National University Hospital, 130 Dongdeok-ro, Jung-gu, Daegu 41944, South Korea. [8]School of Energy and Chemical Engineering, Ulsan National Institute of Science and Technology (UNIST), Ulsan 44919, Republic of Korea.
*These authors contributed equally to this work.
†Corresponding author. Email: jang-ung@yonsei.ac.kr (J.-U.P.); okeye@knu.ac.kr (H.K.K.)

of the sensing data to the user's portable device such as a smartphone or a smartwatch, thereby providing a noninvasive diagnosis of OSI. Also, the patient can build a database for personal health status from this quantitative analysis of MMP-9 during the user's daily activities while wearing the contact lens. Second, as a wireless therapeutic device, a stretchable and transparent heat patch that can be attached on the eyelid area conformably was fabricated using random networks of ultralong metal nanofibers with low sheet resistance and high transmittance. This therapeutic device is small and light enough to avoid interfering with the patient's movement during thermal therapy. Warming the upper and lower eyelids relieves the symptoms of MGD, one of the common pathologies of OSI, by facilitating the lipid expression out of the meibomian gland and stabilizing the tear film. Third, by integrating the smart contact lens (the diagnostic device) and the skin-attachable heat patch (therapeutic device) through wireless communications using a smartphone, the diagnosis-therapy smart health care system can be realized during the wear's outdoor activities, providing personal point-of-care management. Compared with previous studies on smart contact lenses that mainly focus on the diagnosis of diabetes or glaucoma by monitoring glucose or intraocular pressure levels, this system demonstrates the quantitative diagnosis of OSI disease (by detecting MMP-9 concentrations in tears) and the consistent treatment of this symptom; table S2 summarizes the differences of this work from previous studies.

RESULTS

Stretchable, transparent electrodes using ultralong metal nanofibers

Figure 1A illustrates the layouts of an integrated system of the diagnostic and therapeutic devices for the real-time monitoring and therapy of chronic OSI. This system consists of two parts, i.e., (i) a soft, smart contact lens where a graphene FET biosensor, wireless antennas, capacitors, resistors, and an NFC chip are integrated through stretchable interconnects, and (ii) a stretchable and transparent heat patch that can be attached to the patient's eyelid. Figure S1 provides the detailed fabrication method of this contact lens, and fig. S2 shows optical micrographs of the sample for each fabrication step. Sensing signals from the smart contact lens can provide diagnostic data to the user's smartphone wirelessly, and the successive operations allow the heat patch to treat the symptom immediately under controlled temperatures. Because this soft contact lens and the skin-attachable device need to be deformed during their operation, these two wearable devices require sufficient stretchability to ensure reliable operations. Also, the smart contact lens needs to have good transparency with its design to avoid interfering with the wearer's vision. Similarly, high transparency of the heat patch is desired by considering its attachment to the face, especially the eyelid region. Using an electrospinning method, continuous networks of one-dimensional ultralong silver nanofibers (AgNFs) with average diameter of 345 ± 30 nm were formed after thermal annealing at 150°C for 30 min as stretchable and transparent electrodes that were used for the fabrications of device components, including the antenna, joule heating film, and interconnects. The single fibers were long enough to minimize the number of junctions between one-dimensional metallic geometries, which can lead to a substantial reduction in sheet resistance (R_s) while maintaining large open spaces in the networks for high transmittance (27, 28). Figure 1B

shows R_s and transmittance (T) of the AgNF networks as a function of the area fraction. The R_s value of 1.3 ohms per square, with a transmittance of 90% in the visible wavelength regime obtained, which was significantly lower than the R_s of previous transparent conductive films such as indium tin oxide (ITO), chemical vapor deposition (CVD)–synthesized graphene, or random networks of metallic nanowires (29–31). Figure 1 (C and D) shows that the transparent electrodes of AgNF random networks coated on a 25-μm-thick transparent polyimide film (for the bending test) or a 100-μm-thick polydimethylsiloxane (PDMS) film (for stretching) also exhibit outstanding stability against mechanical deformations, including no significant change in resistance down to the bending radius (~70 μm) or high stretchability up to ~80% of tensile strain, which is suitable for their use in the soft contact lens and in the skin-attachable device. However, the large open areas of AgNF networks can significantly increase their resistance when they are patterned as fine electrodes with narrow widths because locally disconnected areas are produced by etching AgNFs (32). To provide additional conductive pathways, therefore, a suspension of silver nanowires (AgNWs) with relatively short lengths and thin diameters (average length, 30 ± 5 μm; diameter, 25 ± 5 nm) were spun directly on top of the electrospun AgNF networks for the narrow patterns of transparent electrodes for the antennas of the smart contact lens. Figure 1E shows scanning electron microscopy (SEM) images of the hybrid electrode networks. Among various wireless communication technologies, NFC can be suitable for smart contact lenses due to the battery-free operations based on the wireless power transfer. The resonant frequency of this NFC platform has been standardized worldwide at 13.56 MHz. Figure 1F shows photographs of the nine-turn NFC antennas (inner diameter of the coil, 4.65 mm; outer diameter, 11.5 mm; antenna width, 300 μm; turn space, 50 μm) fabricated using the copper electrode (Cu thickness, 500 nm) and the AgNF-AgNW hybrid electrode. Compared with the Cu antenna, the antenna sample using this hybrid electrode presented higher transparency (~70% in the visible wavelength regime). This AgNF-AgNW antenna exhibited an impedance of 55 ohms and inductance of 0.7 μH, which fully satisfied the condition of standardized NFC operations, i.e., 0.3 to 3 μH (33). The average diameters of AgNFs and AgNWs were 345 ± 30 and 25 ± 5 nm, respectively. A simulation of the resonant frequency of 13.56 MHz was performed using the ANSYS program, and Fig. 1G plots this simulation result and resonance curves of these two antenna samples fabricated using the Cu and AgNF-AgNW hybrid. The difference between the reflection values (S11) of the Cu and AgNF-AgNW samples was not significant, exhibiting similar impedance values near the resonance frequency of 13.56 MHz (fig. S3). At 10 mm of a transmittance distance, the AgNF-AgNW antenna and the Cu antenna had quality (Q) factors of ~7.9 and ~9.0, respectively, suggesting their high-frequency selectivity. In addition, this AgNF-AgNW antenna showed the negligible change in its resistance under stretching to 30% in tensile strain, which overcomes the limitation of the fragile Cu antenna (Fig. 1H). In case of the inversion of the soft contact lens, the S11 value of the AgNF-AgNW antenna was still maintained (fig. S4). By considering the oxidation of Ag, the AgNF-AgNW antenna was encapsulated with an additional vacuum-deposited parylene layer (thickness, 1 μm). For example, Fig. 1I shows that the smart contact lens maintained its sensing property and wireless communication function after its immersion in a phosphate-buffered saline (PBS) solution and an artificial tear solution for 180 hours.
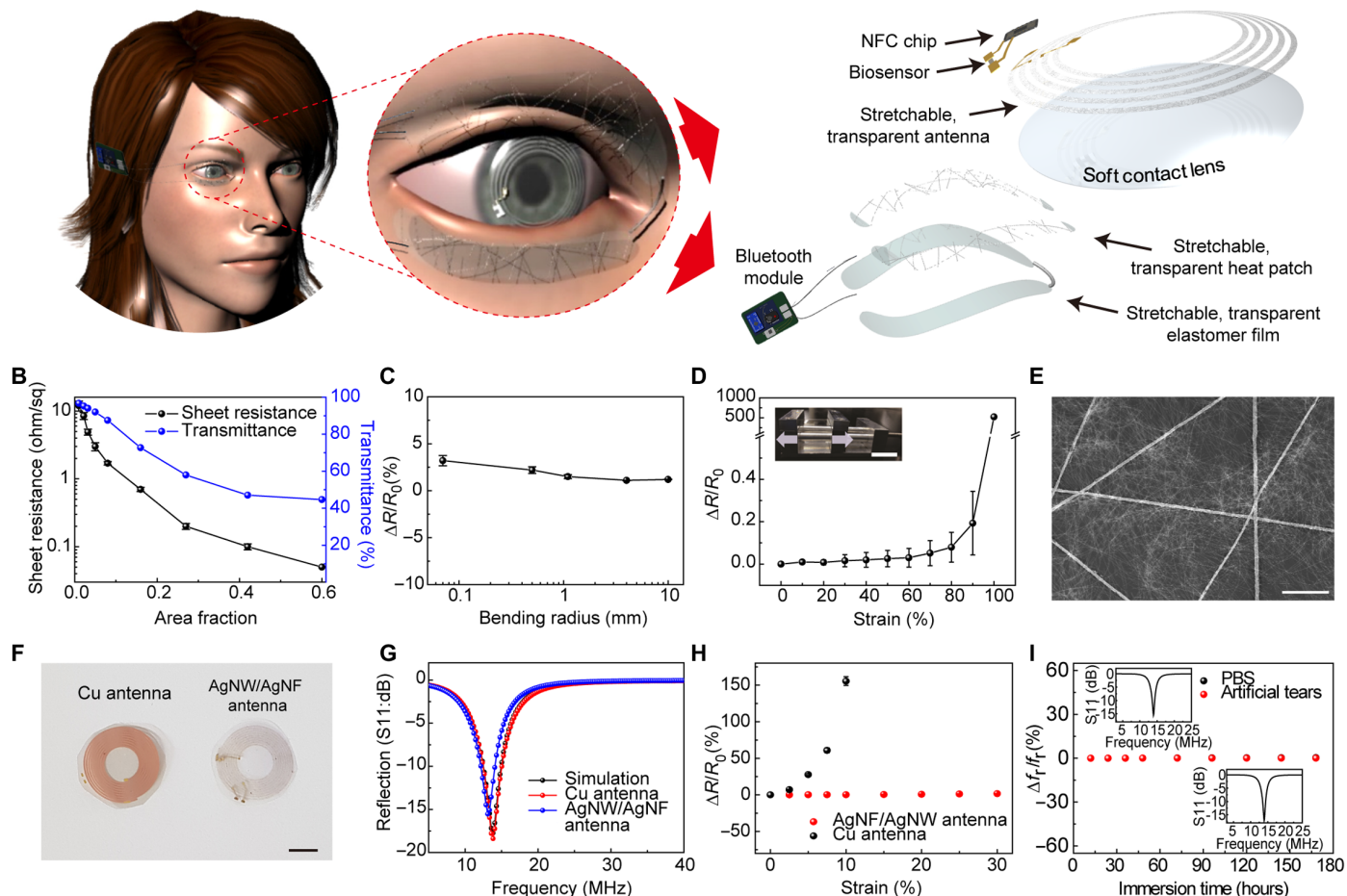
Fig. 1. Stretchable, transparent electrodes using ultralong metal nanofibers. (**A**) Schematic illustrations of the integrated system of the diagnostic and therapeutic devices for the real-time monitoring and therapy of chronic OSI. (**B**) The sheet resistance and optical transmittance as a function of the area fraction of AgNF networks. (**C**) Relative changes in resistance as a function of the radius of curvature. (**D**) Relative changes in resistance as a function of tensile strain. The inset shows the photograph of the experimental setup and the direction of tensile strain application. Scale bar, 1 cm. (**E**) SEM image of AgNF-AgNW hybrid structure. Scale bar, 5 μm. (**F**) Photographs of the antennas that were fabricated on the basis of the Cu electrode (left) and the AgNF-AgNW hybrid (right). Scale bar, 1 mm. (**G**) Inductance-dependent antenna frequencies of two antennas based on the AgNF-AgNW hybrid and Cu electrode with ANSYS simulation. (**H**) Relative changes in resistance of antennas as a function of applied strain. (**I**) Electromagnetic characteristics of the antenna in response to an artificial tear solution and a phosphate-buffered saline (PBS) solution as a function of the immersion time. Inset shows the resonance characteristics of before immersion (top) and after immersion of 180 hours (bottom). Photo credit: (F) Jiuk Jang, Yonsei University.

MMP-9 biosensor for diagnosis of chronic OSI

Diagnosing diseases using biomarkers has been drawing extensive interest for the management of personal health. Among various biomarkers in tear fluids, MMP-9 has been known as an inflammation biomarker of chronic OSI, including DES and MGD (*22, 26*). For detecting the MMP-9 concentration in tears using a smart contact lens, a graphene FET where the graphene surface was functionalized with immunoglobulin G (IgG) was fabricated as a biosensor. To implement a transparent and stretchable structure of this biosensor, the hybrid structure of graphene with random networks of AgNWs was used to form the source and drain electrodes, together with the pristine graphene channel because of the excellent electrical and mechanical properties of the graphene-AgNW hybrid electrodes (*34*). For this fabrication, a CVD-synthesized graphene layer was transferred onto the patterns of AgNW networks before the successive functionalization of the graphene channel with IgG.

Figure 2A shows a schematic image of IgG and its fragments for the antigen-antibody reaction with MMP-9. IgG consists of two antigen-binding fragments (Fab) and one constant fragment (Fc). Since the diameter of the entire IgG antibody was about 10 nm, which is larger than the Debye length, we fragmented IgG antibody into the F(ab′)₂ fragment that contained two antigen-binding sites and an Fc fragment. To ensure that the F(ab′)₂ fragment was isolated, we stained the antigen selectively using a Mix-n-Stain 488A antibody labeling kit (Sigma-Aldrich, USA) and confirmed the fluorescence microscopy of stained F(ab′)₂ fragment as shown in fig. S5. The schematic illustrations of a Fab functionalization and antigen-antibody reactions are presented in Fig. 2B. For the selective detection of MMP-9, the F(ab′)₂ fragment was immobilized on the graphene channel using a pyrene linker from 1-pyrenebutanoic acid succinimidyl ester via π-π stacking, and the succinimidyl ester parts combined with the amino base of the F(ab′)₂ fragment. The
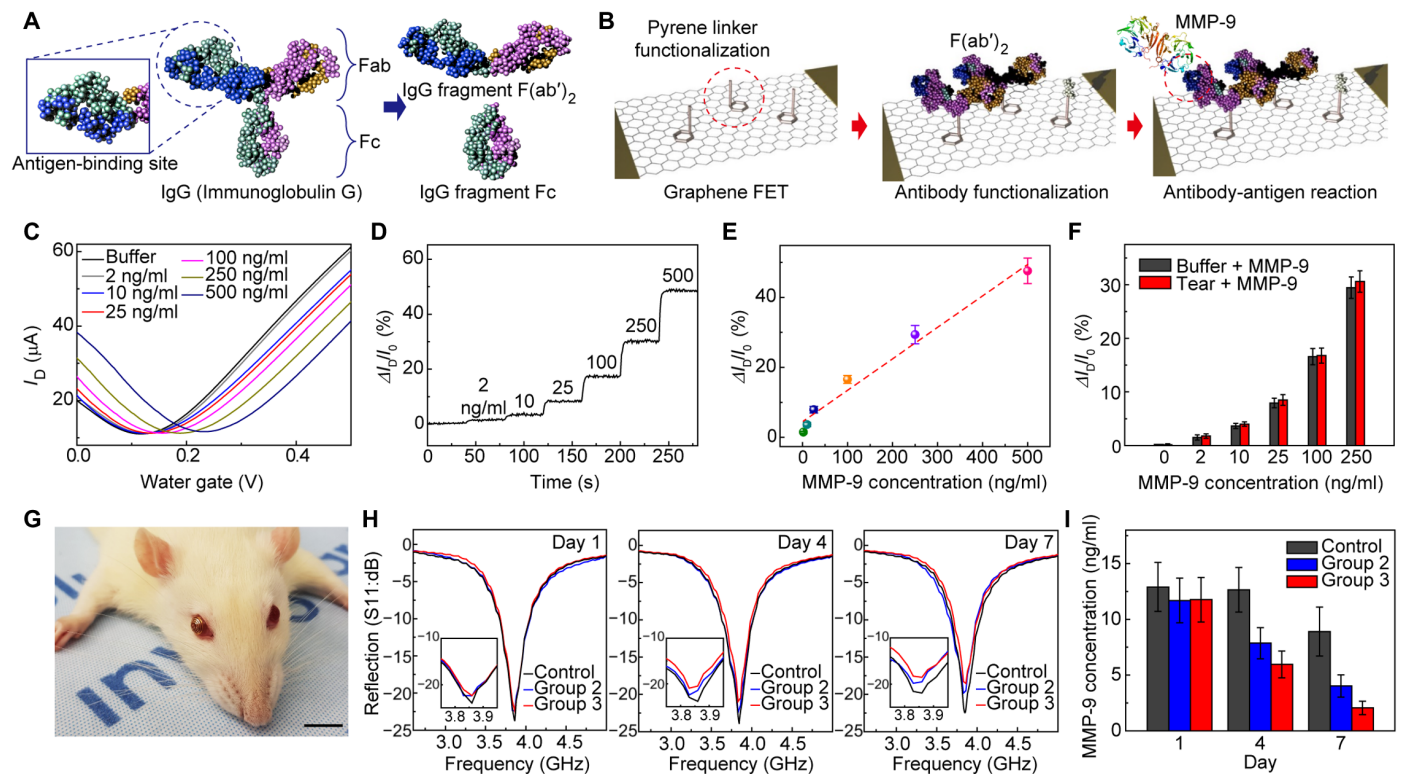
Fig. 2. MMP-9 biosensor and in vivo rat experiment. (**A**) Schematic illustrations of immunoglobulin G (IgG) and its fragments. (**B**) Schematic illustrations of Fab functionalization and antigen-antibody reactions with graphene FET. (**C**) Transfer characteristics (I_D-V_G) of the sensor at various concentrations of MMP-9. (**D**) Real-time, relative changes in drain current at various concentrations of MMP-9 ($V_G = 0$ V, $V_D = 0.1$ V). (**E**) Relative changes in drain current as a function of the concentration of MMP-9. (**F**) Relative changes in drain current with different solutions (black, buffered solution; red, solution of artificial tear). Each data point indicates the average for 10 samples, and error bars represent the SD. (**G**) Photograph of a live Lewis rat wearing the smart contact lens. Scale bar, 2 cm. (**H**) Wireless monitoring of the MMP-9 concentration in each group before (day 1) and after treatment (day 4 and day 7) of OSI. (**I**) Average concentration of MMP-9 in each group during a week ($n = 5$). Photo credit: (G) Jiuk Jang, Yonsei University.

transfer characteristics of graphene FET before and after this functionalization are shown in fig. S6. Then, the MMP-9 can be attached to the antigen-binding site. The transfer characteristics for various concentrations of MMP-9 are shown in Fig. 2C. The CVD-synthesized graphene exhibited ambipolar characteristics, and the drain current increased with the MMP-9 concentration at zero gate bias ($V_G = 0$ V) compared with the buffer-only case, suggesting that the positively charged MMP-9 was attached to the graphene channel. On the basis of the transfer characteristics, the drain current was measured in real time at $V_G = 0$ V for various MMP-9 concentrations from 1 to 500 ng/ml (Fig. 2D). In general, when the concentration of MMP-9 in the tear fluids was 40 ng/ml or more, the person can be considered to have symptoms of chronic OSI, and when the concentration is more than 200 ng/ml, the person is diagnosed as having chronic OSI (*21*). As shown in the calibration curve (Fig. 2E), the sensor was highly responsive to the pathological range of the MMP-9 concentration in tear fluids (1 to 500 ng/ml). The signal-to-noise ratio (SNR) was 8.14 at 2 ng/ml, and the limit of detection (at SNR = 3) was 0.74 ng/ml. The sensitivity (*S*) of this sensor was calculated as 11.1 ng/ml per 1% of the change in its drain current. The response time of the sensor was defined as the time required for the sensor to reach 90% of the detection results, and it was measured as ~2.5 s. The sensitivity was not significantly different for the cases of tear and buffered solutions, as shown in Fig. 2F, which indicate that

other elements in tears affect negligible interference with this MMP-9 sensor. Furthermore, the sensing characteristics were also maintained in a mixture interferent molecules (i.e., ascorbic acid, lactate, and urea), which exhibits the good selectivity of the MMP-9 sensor (fig. S7A). Because human tear fluids have pH ranges from 6.5 to 7.5, we conducted the reliability test of the MMP-9 sensor for various buffer solutions with different pH levels (6.4 to 8.0). As shown in fig. S7B, the pH effect on the sensing performance of this sensor was negligible.

This quantitative measurement of the MMP-9 concentration allows the user to monitor inflammation of the eye in real time. To investigate the long-term stability of the contact lens sensor, we conducted the accelerated aging test at 70°C as the aging temperature. For this test, contact lens sensors were stored in the air for 16 days, which corresponded to the storage period of 1 year. Then, their resonance characteristics were measured using a network analyzer. As shown in fig. S8, the relative change in resonance frequency was negligible.

We applied the smart contact lens to the chronic OSI rat model (*35*) to perform the in vivo validation of this lens device. For this in vivo experiment, we fabricated smart contact lenses fit to the size of a rat's eyeball (average diameter, 5.5 ± 0.3 mm) (*36*), and the detailed fabrication methods are described in Materials and Methods. In this in vivo experiment, OSI was induced to 8-week-old Lewis

rats (weight, 100 to 125 g) by treating 15 rats (30 eyes) with benzalkonium chloride [BAC; 0.2 weight % (wt %)] twice a day (n = 5 for 3 groups). Here, the rats were housed in a controlled environment chamber (CEC), which maintained the conditions of 18.5% RH (relative humidity), 25°C, and an air flow rate of 20 liters/min. We divided the OSI-induced rats into three groups, i.e., the OSI-positive group (control group), a natural healing group (group 2), and a group treated with dexamethasone (group 3, 10 μM, 5 μl, three times per day). To verify the characteristics of the contact lens sensor, the S11 values of the contact lens samples were measured for each group. Figure 2G shows a live rat wearing the lens sensor for the sensing of MMP-9. The change in S11 values for each group with respect to the healing time is provided in Fig. 2H. The calibration graph of the sensor for rats is provided in fig. S9. The S11 values of group 3, which was treated with dexamethasone for the fast recovery of OSI, decreased during the recovery time. Also, Fig. 2I shows the change in MMP-9 concentration with recovery time for each group. The concentration of MMP-9 decreased as the OSI was relieved, suggesting the potentials to use this smart contact lens to diagnose chronic OSI in humans.

Stretchable, transparent heat patch for remote therapy for chronic OSI

The tear fluid is composed of three layers, i.e., a lipid layer, an aqueous layer, and a glycocalyx layer (26). The lipid layer (with a thickness of 15 to 160 nm), which is secreted by the meibomian gland, covers the aqueous layer, preventing the evaporation of moisture. When the gland is damaged, it causes hyperevaporative dryness of the surface of the eye, and the heat treatment of eyelids can be effective for relieving the symptoms of MGD, which is the main cause of OSI, with the normalization of the gland's function (24). However, it is difficult to routinely use conventional thermal therapy equipment because it has bulky components (for example, separated power source and controllers) and the patient's vision is also obscured (25). Although several medical devices, such as Lipiflow (TearScience, Morrisville, NC, USA) and IPL, have been developed for the thermal treatment, there are difficulties in their application in daily life because of the aforementioned limitations. Table S3 summarizes the comparison of our device performance with the cases of recent commercial clinical systems and gold standards. The wearable heat patch can allow the continuous and frequent thermal therapy, thereby providing the convenient treatment for the early and severe OSI disease such as DES.

To overcome these challenges, the stretchable and transparent heat patch attachable to the face conformably was fabricated as a wireless therapeutic device (Fig. 3A). The stretchable and transparent heating film was formed by electrospinning the continuous random networks of AgNFs on an elastomer film (PDMS). The areal dimension of this transparent heat patch was relatively large enough to maintain the conductive pathways along AgNFs without the additional use of AgNWs, which exhibited an R_s of 1.3 ohms per square with a T of 90% in the visible wavelength range. This heating film was then integrated with a Bluetooth module with a microcontroller unit (MCU) (BI-200M, Blueinno, Korea), a commercial temperature sensor (MA100BF103A, Amphenol Advanced Sensors, USA), and a battery (TW-802030, The Han Inc., Korea) for its wireless temperature control. Figure 3B shows a circuit diagram, and a custom-designed circuit program was installed in the MCU to adjust target temperatures automatically using a smartphone. Figure

S10 provides the detailed information of the flexible printed circuit board for the therapeutic device. Figure 3C presents a photograph of a pair of the AgNF-based heat patches attached on the upper and lower eyelid areas of a human subject conformably. The infrared (IR) images of Fig. 3D and movie S1 indicate the reliable operations of this therapeutic device (as a pair) with the wireless control of temperatures for the hyperthermia treatment. The temperature of the heat patch varies depending on the applied dc bias (Fig. 3E). From the temperature profile in this figure, the thermal conductivity of this AgNF heat patch was calculated as 109.1 W/m·K. Figure S11 compares the properties of this AgNF heat patch with those of other transparent heaters based on the ITO (R_s, ~50 ohms per square) and AgNWs (R_s, ~10 ohms per square). All of these three heaters were fabricated on polyimide films, and they had the same optical transmittance (85%). The relatively low R_s of this AgNF heat patch enabled it to pass relatively large currents at an identical input dc bias, resulting in its effective power consumption. Also, the heater based on AgNF networks exhibited the rapidest heating and cooling rate among these three heaters. Furthermore, as shown in Fig. 3F, the temperature remained constant at the target temperature (blue dashed line in the graph) through the feedback from the temperature sensor in the closed loop. To avoid low-temperature burn, this therapeutic device was programmed to not exceed 45°C. The power consumption of this heat patch was 0.24 mW, and the maximum operation time was 200 min. Figure 3 (G and H) shows the mechanical properties of this AgNF heat patch under deformations such as bending and stretching. The temperature was constantly maintained by bending it down to the minimum bending radius of 70 μm and by stretching it up to 90% in tensile strain. In addition, the temperature change was negligible (~2%) even after 10,000 cycles of repetitive stretching at 30% strain, which implies that this AgNF heat patch can be suitable for the human skin (Fig. 3I). Also, Fig. 3J plots its reliable operation during the cyclic on-off settings.

Remote monitoring and treatment

Figure 4A demonstrates the integrated system of the smart contact lens (as the diagnostic device) with eyelid-attachable heat patch (as therapeutic device) through wireless communications using a smartphone. Sensing signals from the contact lens are processed with the smartphone, and then wireless operations are executed to the eyelid-attached heat patches instantly. Figure 4B shows a photograph of this contact lens, and the inset presents a live rabbit wearing it. For the fabrication of this contact lens, an Si-based logic bare die (RF430FRL152H, Texas Instruments, USA) NFC chip was integrated with the AgNF-AgNW antenna, resistors, and capacitors to digitize the measured data and transmit the information to the smartphone. We implemented highly transparent and stress-tunable hybrid geometries composed of rigidly reinforced islands using a thin, photo-patternable optical polymer (SPC-414, EFiRON) for locating fragile components (such as NFC chip, MMP-9 sensor, capacitor, and resistors), and soft matrix for locating the AgNF-AgNW antenna and interconnection electrodes. Electrical components of the smart contact lens were connected electrically through stretchable interconnections, which were directly printed using a liquid metal of an eutectic gallium-indium alloy as the ink (EGaIn, 75 wt % Ga and 25 wt % In, Changsha Santech Materials Co. Ltd.) with a narrow linewidth (<10 μm) (37, 38). These device components located on an elastomeric film can be molded into a contact lens shape
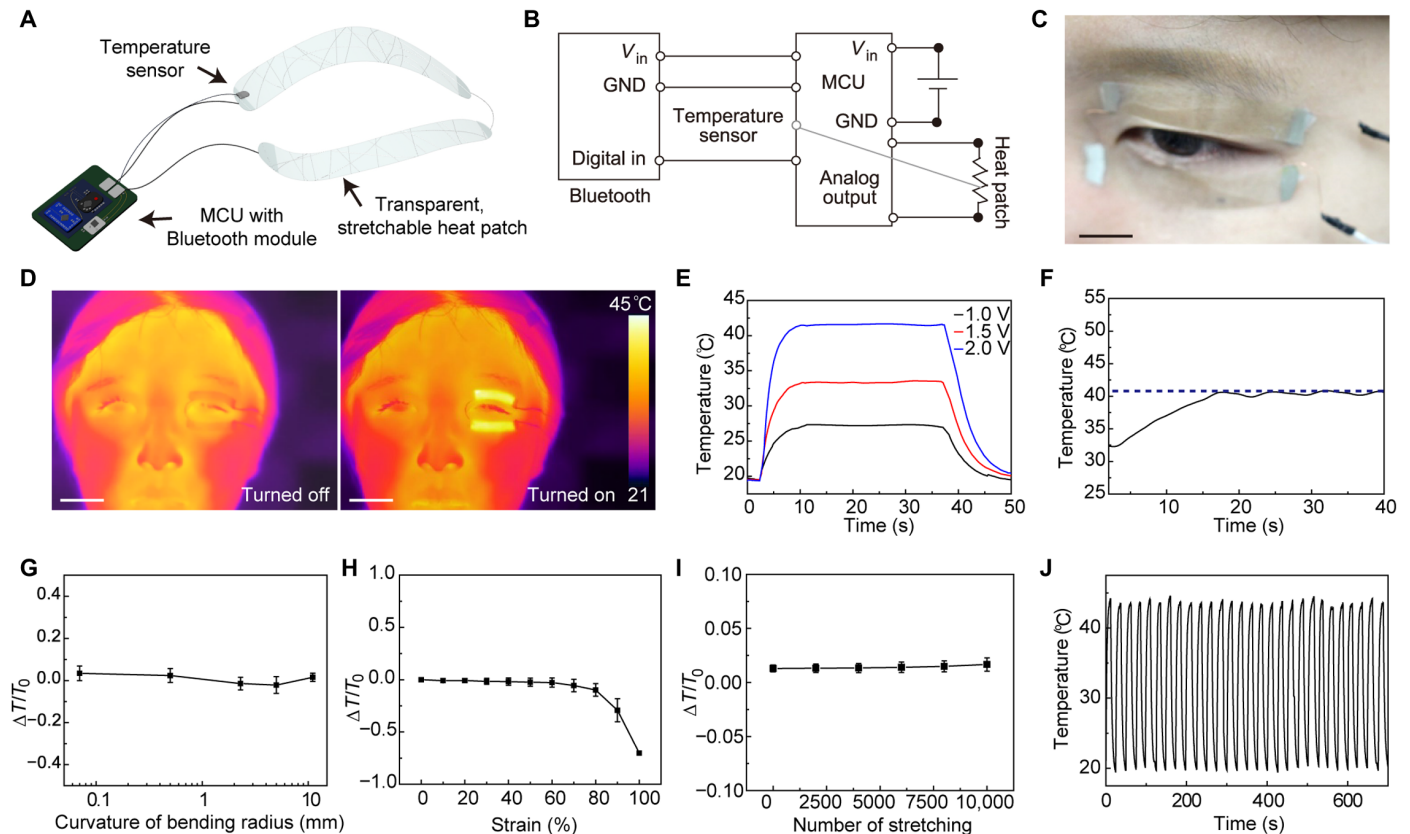
Fig. 3. Stretchable, transparent heat patch for remote hyperthermia treatment. (**A**) Schematic illustrations of the wireless therapeutic device. (**B**) Circuit diagram of the heat patch, microcontroller unit (MCU), and Bluetooth module. (**C**) Photograph of the stretchable and transparent heat patch attached on the upper and lower eyelid areas of human subject. Scale bar, 1 cm. (**D**) Infrared (IR) images of the heat patch before (left) and during the operation (right). Scale bars, 3 cm. (**E**) The temperature of the heat patch as a function of the time for different dc bias (1, 1.5, and 2 V). (**F**) The temperature of the heat patch as a function of the time with automatic feedback from the temperature sensor and MCU. The blue dashed line indicates target temperature. (**G** and **H**) Relative change in the temperature as a function of radius of curvature (G) and tensile strain (H). (**I**) Relative change in the temperature after repetitive stretching (~30% of tensile strain). (**J**) Thermal stability test during the cyclic on-off settings of the heat patch. The plot indicates the average temperature of the heat patch as a function of time. Photo credit: (C) Jiuk Jang, Yonsei University.

using a conventional soft lens material (elastofilcon A, CooperVision, USA), as shown in fig. S12. The resonance characteristic of the contact lens sensor was maintained before and after lens molding process (fig. S13). Figure 4C presents a rabbit wearing a pair of the AgNF-based heat patches attached to the rabbit's upper and lower eyelid areas.

Figure 4D demonstrated the detection of MMP-9 concentration and the instantaneous temperature control of the heat patch, which operated automatically based on the sensing data that were acquired for the concentration of MMP-9. As the graphene FET biosensor detected the concentration of MMP-9 in an artificial tear solution, the smart contact lens transmitted this signal to a smartphone through NFC. Figure S14 shows this circuit diagram. When the transmitted signal exceeded the threshold (concentration of MMP-9, ≥200 ng/ml), the home-built smartphone application immediately sent a treatment command to the therapeutic device, allowing the heat patch to operate at the specific therapy temperature (42°C). MGD, which is a commonly underlying pathology in OSI, can be cured by this hyperthermia treatment (*24*). For the in vivo validation of this system, we administered BAC (0.1 wt %) to the rabbit's eyes (*39*), arranging the rabbit OSI model (Fig. 4E). The experimental group (i.e., the group that was treated with BAC) showed ~4 times

higher concentration of MMP-9 than the untreated control group. Figure 4F shows a live rabbit wearing both the contact lens and the therapeutic device for their wireless controls. After wearing the lens, the rabbit showed no signs of abnormal behaviors, and this lens maintained its position stably during its repeated eye blinks (movie S2). As the smartphone got closer to the rabbit's eye, the sensing signal was processed and then displayed on the smartphone screen. Because the rabbit was treated with BAC (i.e., the concentration of MMP-9 in tear fluids, ≥250 ng/ml), the automatic operation of the heat patch was executed (Fig. 4G). As shown in movie S2, the heat patch provided a stable and uniform temperature distribution. Also, the temperature of this lens device and that of the sclera of the rabbit were reliably maintained at approximately 37° and 38°C, respectively, without any significant generation of heat during the power transfer from the transmitting coil (fig. S15, A and B). The relative change in the signal of MMP-9 concentration during the blinking of the rabbit's eye was negligible, suggesting the stable wireless operation of the contact lens sensor (fig. S15C).

In vivo human pilot study

Figure 5A and movie S3 demonstrate a 27-year-old human female subject wearing this soft, smart contact lens, which can wirelessly
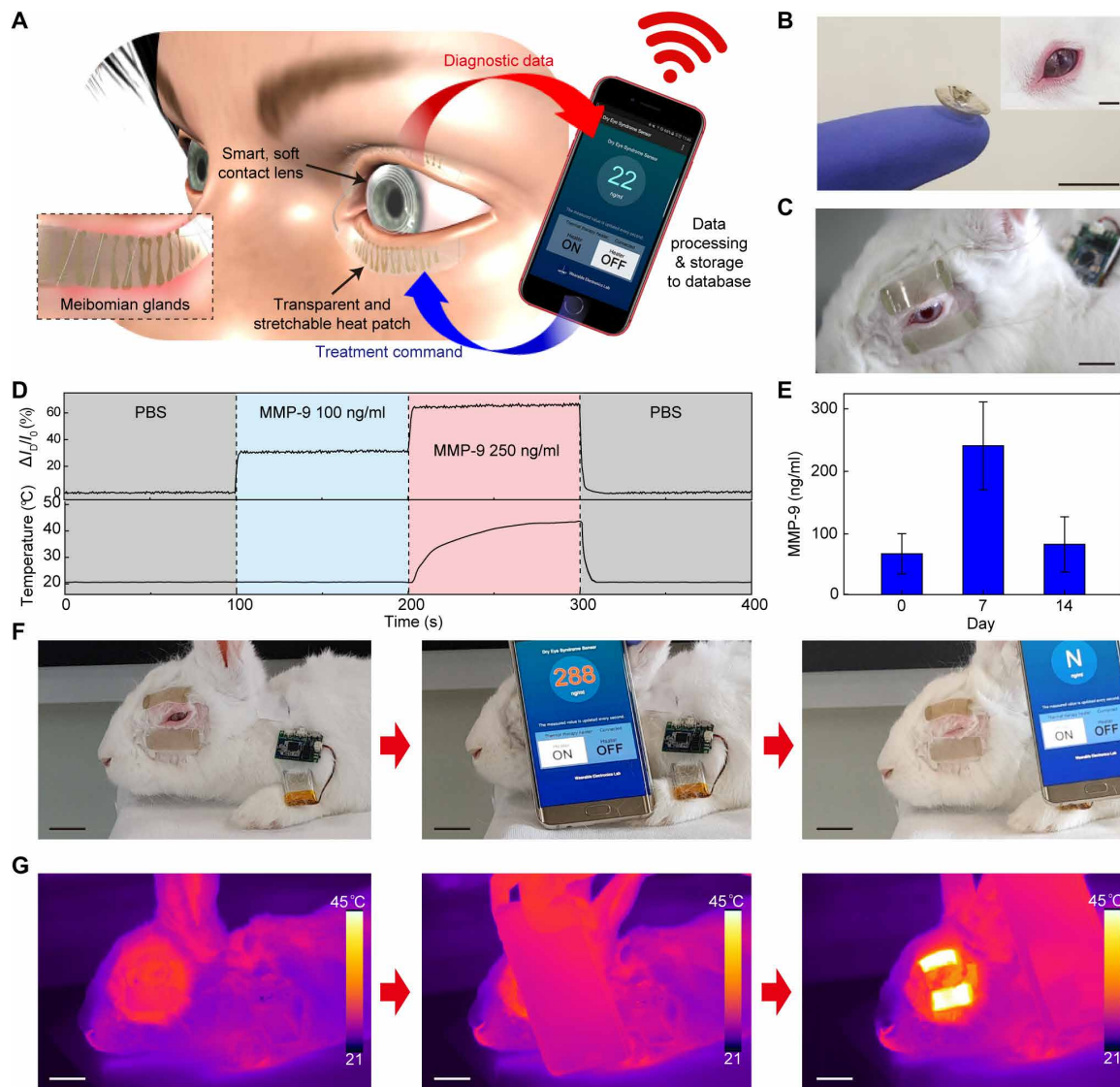
Fig. 4. Remote monitoring and treatment of chronic OSI. (**A**) Schematic illustration of operation algorithms for integrated system that consists of the soft, smart contact lens (diagnostic device), the eyelid-attachable heat patch (therapeutic device), and the smartphone (wireless communication). (**B**) Photograph of soft, smart contact lens. Scale bar, 2 cm. The inset shows the live rabbit wearing the soft contact lens. Scale bar, 1 cm. (**C**) A photograph of a rabbit wearing a pair of the AgNF-based heat patches attached to the rabbit's upper and lower eyelid areas. Scale bar, 2 cm. (**D**) Detection of MMP-9 concentration and the instantaneous temperature control of the heat patch. Each plot shows real-time changes of the relative drain current of the contact lens (top) and the temperature of the heat patch (bottom). (**E**) Concentration of MMP-9 in the tears of the live rabbit after treatment with 0.1 wt% BAC ($n = 5$). (**F**) Photographs of the live rabbit during the in vivo examination. Left: A live rabbit wearing the smart contact lens and therapeutic device simultaneously. Middle: A smartphone receives the sensing signals from the smart contact lens via NFC and issues the operation commands to the therapeutic device. Right: The therapeutic device is on the operation. Scale bars, 3 cm. (**G**) IR images of the live rabbit during the in vivo examination. Each IR image corresponds to the photographs in (F). Scale bars, 3 cm. Photo credit: (B, C, and F) Jiuk Jang, Yonsei University.

transmit the concentration of MMP-9 in tears to a smartphone. When the smartphone was placed near the contact lens, the data transmitted from the lens were displayed on the screen (23 ± 1 ng/ml) in real time. The real-time measurement of the MMP-9 concentration can be a primary endpoint of this human pilot trial. To provide the reliability of this contact lens device, MMP-9 concentration was measured for multiple subjects as pilot trials, and the average concentration of MMP-9 was 29.1 ± 5.0 ng/ml ($n = 4$). To verify the safety of the wearer from electromagnetic waves, we performed the simulation for a specific absorption rate (SAR) for a person with the

ANSYS program (Fig. 5B). Here, the maximum SAR value of this lens system was 1.0 W/kg, which was lower than the standard regulation (10 W/kg). Furthermore, the cytotoxicity of this smart contact lens was tested by measuring the viability of cells from mouse fibroblasts (fig. S16). Detailed protocols were described in Materials and Methods. The graph shows that the cell viability was 82%, which was comparable to the case of commercial soft contact lenses that included no electronic devices, suggesting that our smart contact lens was not significantly cytotoxic. Figure 5C shows a magnified photograph of the eye of this human subject who was wearing
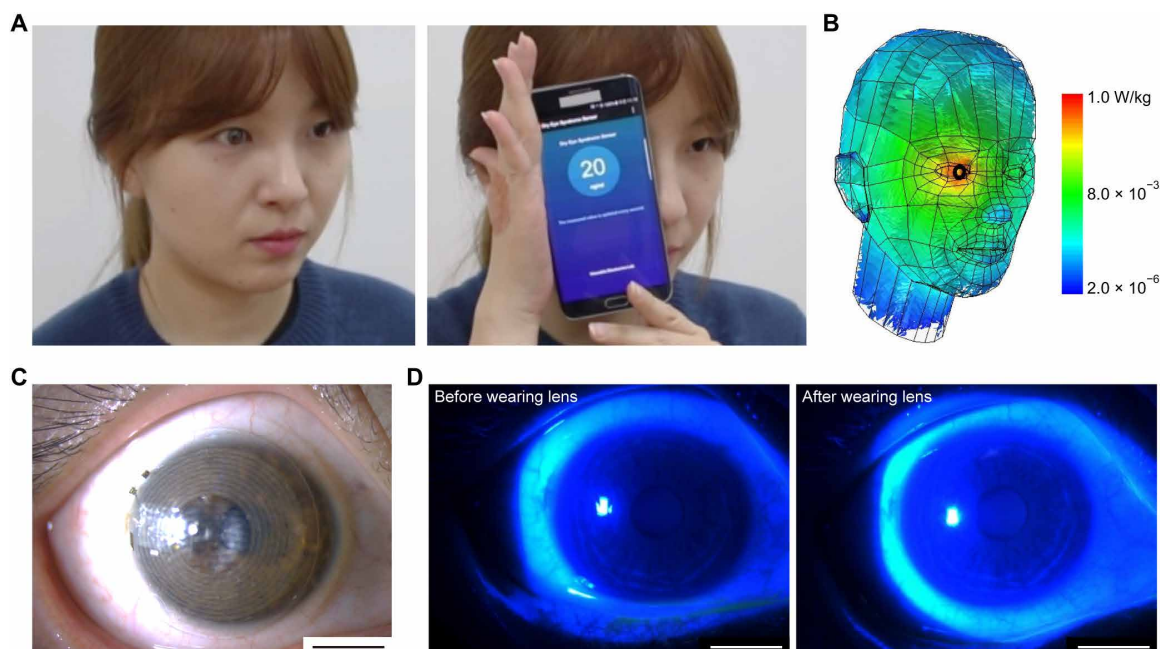
Fig. 5. In vivo human study of the soft, smart contact lens. (A) Photographs of a human female subject wearing the soft, smart contact lens before measurement (left) and during the measurement using a smartphone (right). (**B**) Specific absorption rate (SAR) simulation result at 13.56 MHz for the extreme environmental case, in which there is a current flow of 1.2 A in the contact lens. (**C**) Magnified photograph of the eye of human subject wearing the smart contact lens. Scale bar, 0.5 cm. (**D**) Series of immunofluorescence images of the human eye before wearing the contact lens (left) and after wearing the contact lens for 12 hours (right). Scale bars, 0.5 cm. Photo credit: (A and C) Jiuk Jang, Yonsei University.

this lens, indicating that there was no serious inflammation of the eye. All the electronic components were placed outside the pupil to minimize the interference with the subject's field of vision. After wearing this lens for 12 hours, a slit lamp examination was conducted on the subject's eye. Figure 5D shows fluorescence images of the cornea of this human subject before and after wearing the contact lens, and the images indicate that there was no apparent reaction of the cornea to this lens. Also, the conjunctival area of the female subject's eye was examined before and after 12 hours of wearing the smart contact lens, and no conjunctival injection was observed after wearing (fig. S17). In addition, we measured the concentration of MMP-9 before and after 2 weeks of thermal treatment using our heat patch (once a day, 15 min) for the subject who showed high concentration of MMP-9. As shown in fig. S18, the concentration of MMP-9 decreased after 2 weeks, suggesting the substantial potential of this system.

DISCUSSION

We demonstrated the wireless integration of a diagnostic device and a therapeutic device for the real-time monitoring and therapy of chronic OSI using mobiles. The system consists of a soft, smart contact lens as a diagnostic device that can detect the concentration of MMP-9 in tear fluids, as well as a transparent and stretchable heat patch that can be attached to the eyelid conformably as a therapeutic device for the hyperthermia treatment. The smart contact lens enables the real-time detection of the MMP-9 concentration in tears using a graphene FET biosensor. The heat patch fabricated using continuous random networks of AgNFs presents effective power consumptions with good stretchability and transparency

suitable for the eyelid skin with negligible irritations. Both diagnostic and therapeutic devices were incorporated through wireless communications with programmed applications, enabling instantaneous and automated hyperthermia treatments of the heat patch based on the signals detected from the contact lens. The in vivo experiments using live animals and human subjects confirm their good wearability and reliability as a noninvasive, mobile health care solution. This personal point-of-care system can provide new opportunities to clinical information and the potential capability for machine learning in diagnosing disease. Clinical analyses on the correlation of the chronic OSI level in the tears with other biomarkers at various physiological conditions appear to be a promising direction for future work.

MATERIALS AND METHODS
Rat experiment
All animals were maintained and used in accordance with the Guidelines for the Care and Use of Laboratory Animals of the Institute of Laboratory Animal Center, Daegu-Gyeongbuk Medical Innovation Foundation. The animal studies were conducted after approval by the institutional reviewer board of the Ethics of Animal Experiments of the Daegu-Gyeongbuk Medical Innovation Foundation (DGMIF-19052204-00). An OSI was induced to 8-week-old Wisker rats by treatment with BAC (0.2 wt %) twice a day on 30 eyes (*n* = 5 for 3 groups). During the experiment, the rats were stored in a CEC, which was maintained at 18.5% RH, 25°C, and 20 liters/min of air flow rate. We divided OSI-induced rats into three groups, such as OSI positive (control group), natural healing group (group 2), and dexamethasone (10 µM, 5 µl, three times per day)–treated group (group 3).

Cell viability test of soft, smart contact lenses

Normal human dermal fibroblast cells (Promocell) were maintained in Cascade Biologics Medium 106 (Gibco), supplemented with Low Serum Growth Supplement (Gibco) (complete medium) at 37°C in a humidified atmosphere of 5% CO_2 with medium change every 3 days. When the confluence was closed in 80%, the cells were subcultured with 0.025% trypsin/EDTA (Gibco) and incubated in the complete medium condition. At fourth passage, these cells were harvested and plated at a density of 5000 cells per well in each well of 96 well plates. The cells were incubated in complete medium for 24 hours.

For the cytotoxicity test, the process was performed in accordance with ISO 10993-5. In this experiment, smart contact lens was compared in both polyurethane films containing 0.1% zinc diethyldithiocarbamate (Hatano Research Institute) and high-density polyurethane film (Hatano Research Institute) as a positive and negative control, respectively. Before the experiment, all contact lenses were sterilized in 70% ethanol for 30 min, and the samples were then dried in fume hood. Each sample ($n = 4$) was immersed and incubated in complete medium at 37°C for 48 hours. The condition for extracts was prepared with contact lens of 0.2 g in complete medium of 1 ml. The pretreated medium of incubated cells was changed to extracted medium immersed with contact lenses. The cells treated with extracted medium were incubated for 24 hours. The cytotoxicity was assessed by a cell counting kit-8 assay (Dojindo). The absorbance was read at 450 nm using a multimode plate reader (PerkinElmer). The absorbance values were converted into percentage values of the blank obtained from only cell growth media.

Human pilot study

The protocol for this study was approved by the Institutional Review Board of the Ulsan National Institute of Science and Technology (UNISTIRB-18-17-A). All experiments and trials were carried out with the full, informed consent of the volunteer. Thermal treatment on the human subjects was performed using a heat patch once a day for 15 min for 2 weeks. The soft, smart contact lens was rinsed with contact lens cleansing solution (Frenz-pro B5 solution, JK Pharmaceutical Inc., Korea), followed by PBS for 1 min before wearing. After the human trial, the ocular surface of the volunteer was evaluated using the slit lamp examination (SL-15, Kowa Optimed Inc., Japan).

SUPPLEMENTARY MATERIALS

Supplementary material for this article is available at http://advances.sciencemag.org/cgi/content/full/7/14/eabf7194/DC1

REFERENCES AND NOTES

1. D.-H. Kim, N. Lu, R. Ma, Y.-S. Kim, R.-H. Kim, S. Wang, J. Wu, S. M. Won, H. Tao, A. Islam, K. J. Yu, T. Kim, R. Chowdhury, M. Ying, L. Xu, M. Li, H.-J. Chung, H. Keum, M. McCormick, P. Liu, Y.-W. Zhang, F. G. Omenetto, Y. Huang, T. Coleman, J. A. Rogers, Epidermal electronics. *Science* **333**, 838–843 (2011).

2. W. Gao, S. Emaminejad, H. Y. Y. Nyein, S. Challa, K. Chen, A. Peck, H. M. Fahad, H. Ota, H. Shiraki, D. Kiriya, D.-H. Lien, G. A. Brooks, R. W. Davis, A. Javey, Fully integrated wearable sensor arrays for multiplexed in situ perspiration analysis. *Nature* **529**, 509–514 (2016).

3. J. Xiong, G. Thangavel, J. Wang, X. Zhou, P. S. Lee, Self-healable sticky porous elastomer for gas-solid interacted power generation. *Sci. Adv.* **6**, eabb4246 (2020).

4. V. Nair, J. Yi, D. Isheim, M. Rotenberg, L. Meng, F. Shi, X. Chen, X. Gao, A. Prominski, Y. Jiang, J. Yue, C. T. Gallagher, D. N. Seidman, B. Tian, Laser writing of nitrogen-doped silicon carbide for biological modulation. *Sci. Adv.* **6**, eaaz2743 (2020).

5. K. Sim, Z. Rao, H.-J. Kim, A. Thukral, H. Shim, C. Yu, Fully rubbery integrated electronics from high effective mobility intrinsically stretchable semiconductors. *Sci. Adv.* **5**, eaaz5749 (2019).

6. Y. Ai, T. H. Hsu, D. C. Wu, L. Lee, J.-H. Chen, Y.-Z. Chen, S.-C. Wu, C. Wu, Z. M. Wang, Y.-L. Chueh, An ultrasensitive flexible pressure sensor for multimodal wearable electronic skins based on large-scale polystyrene ball@reduced graphene-oxide core–shell nanoparticles. *J. Mater. Chem. C* **6**, 5514–5520 (2018).

7. Y. J. Yoo, W.-G. Kim, J. H. Ko, Y. J. Kim, Y. Lee, S. G. Stanciu, J.-M. Lee, S. Kim, J.-W. Oh, Y. M. Song, Large-area virus coated ultrathin colorimetric sensors with a highly lossy resonant promoter for enhanced chromaticity. *Adv. Sci.* **7**, 2000978 (2020).

8. F. Ershad, A. Thukral, J. Yue, P. Comeaux, Y. Lu, H. Shim, K. Sim, N.-I. Kim, Z. Rao, R. Guevara, L. Contreras, F. Pan, Y. Zhang, Y.-S. Guan, P. Yang, X. Wang, P. Wang, X. Wu, C. Yu, Ultra-conformal drawn-on-skin electronics for multifunctional motion artifact-free sensing and point-of-care treatment. *Nat. Commun.* **11**, 3823 (2020).

9. J. Jang, H. Kim, S. Ji, H. J. Kim, M. S. Kang, T. S. Kim, J.-e. Won, J.-H. Lee, J. Cheon, K. Kang, W. B. Im, J.-U. Park, Mechanoluminescent, air-dielectric MoS_2 transistors as active-matrix pressure sensors for wide detection ranges from footsteps to cellular motions. *Nano Lett.* **20**, 66–74 (2020).

10. J. Jang, B. Oh, S. Jo, S. Park, H. S. An, S. Lee, W. H. Cheong, S. Yoo, J.-U. Park, Human-interactive, active-matrix displays for visualization of tactile pressures. *Adv. Mater. Technol.* **4**, 1900082 (2019).

11. J. Jang, Y. S. Jun, H. Seo, M. Kim, J.-U. Park, Motion detection using tactile sensors based on pressure-sensitive transistor arrays. *Sensors* **20**, 3624 (2020).

12. J. Kim, M. Kim, M.-S. Lee, K. Kim, S. Ji, Y.-T. Kim, J. Park, K. Na, K.-H. Bae, H. Kyun Kim, F. Bien, C. Young Lee, J.-U. Park, Wearable smart sensor systems integrated on soft contact lenses for wireless ocular diagnostics. *Nat. Commun.* **8**, 14997 (2017).

13. J. Park, J. Kim, S.-Y. Kim, W. H. Cheong, J. Jang, Y.-G. Park, K. Na, Y.-T. Kim, J. H. Heo, C. Y. Lee, J. H. Lee, F. Bien, J.-U. Park, Soft, smart contact lenses with integrations of wireless circuits, glucose sensors, and displays. *Sci. Adv.* **4**, eaap9841 (2018).

14. J. Park, D. B. Ahn, J. Kim, E. Cha, B.-S. Bae, S.-Y. Lee, J.-U. Park, Printing of wirelessly rechargeable solid-state supercapacitors for soft, smart contact lenses with continuous operations. *Sci. Adv.* **5**, eaay0764 (2019).

15. J. Kim, E. Cha, J.-U. Park, Recent advances in smart contact lenses. *Adv. Mater. Technol.* **5**, 1900728 (2020).

16. Y.-G. Park, E. Cha, H. S. An, K.-P. Lee, M. H. Song, H. K. Kim, J.-U. Park, Wireless phototherapeutic contact lenses and glasses with red light-emitting diodes. *Nano Res.* **13**, 1347–1353 (2020).

17. P. Tseng, B. Napier, L. Garbarini, D. L. Kaplan, F. G. Omenetto, Functional, RF-trilayer sensors for tooth-mounted, wireless monitoring of the oral cavity and food consumption. *Adv. Mater.* **30**, e1703257 (2018).

18. Y. Liu, M. Pharr, G. A. Salvatore, Lab-on-skin: A review of flexible and stretchable electronics for wearable health monitoring. *ACS Nano* **11**, 9614–9635 (2017).

19. N. L. Lanza, F. Valenzuela, V. L. Perez, A. Galor, The matrix metalloproteinase 9 point-of-care test in dry eye. *Ocul. Surf.* **14**, 189–195 (2016).

20. E. M. Messmer, The pathophysiology, diagnosis, and treatment of dry eye disease. *Dtsch. Arztebl. Int.* **112**, 71–82 (2015).

21. K. K. Nichols, J. J. Nichols, M. Mph, G. L. Mitchell, The lack of association between signs and symptoms in patients with dry eye disease. *Cornea* **23**, 762–770 (2004).

22. A. Acera, E. Vecino, J. A. Duran, Tear MMP-9 levels as a marker of ocular surface inflammation in conjunctivochalasis. *Invest. Ophthalmol. Vis. Sci.* **54**, 8285–8291 (2013).

23. S. Chotikavanich, C. S. de Paiva, D. Q. Li, J. J. Chen, F. Bian, W. J. Farley, S. C. Pflugfelder, Production and activity of matrix metalloproteinase-9 on the ocular surface increase in dysfunctional tear syndrome. *Invest. Ophthalmol. Vis. Sci.* **50**, 3203–3209 (2009).

24. J. V. Greiner, Long-term (12-month) improvement in meibomian gland function and reduced dry eye symptoms with a single thermal pulsation treatment. *Clin. Experiment. Ophthalmol.* **41**, 524–530 (2013).

25. M. J. Kim, S. S. Stinnett, P. K. Gupta, Effect of thermal pulsation treatment on tear film parameters in dry eye disease patients. *Clin. Ophthalmol.* **11**, 883–886 (2017).

26. G. N. Foulks, A. J. Bron, Meibomian gland dysfunction: A clinical scheme for description, diagnosis, classification, and grading. *Ocul. Surf.* **1**, 107–126 (2003).

27. J. Jang, B. G. Hyun, S. Ji, E. Cho, B. W. An, W. H. Cheong, J.-U. Park, Rapid production of large-area, transparent and stretchable electrodes using metal nanofibers as wirelessly operated wearable heaters. *NPG Asia Mater.* **9**, e432 (2017).

28. S. Lee, S.-W. Kim, M. Ghidelli, H. S. An, J. Jang, A. L. Bassi, S.-Y. Lee, J.-U. Park, Integration of transparent supercapacitors and electrodes using nanostructured metallic glass films for wirelessly rechargeable, skin heat patches. *Nano Lett.* **20**, 4872–4881 (2020).

29. X. Li, W. Cai, J. An, S. Kim, J. Nah, D. Yang, R. Piner, A. Velamakanni, I. Jung, E. Tutuc, S. K. Banerjee, L. Colombo, R. S. Ruoff, Large-area synthesis of high-quality and uniform graphene films on copper foils. *Science* **324**, 1312–1314 (2009).

30. J.-U. Park, S. Nam, M.-S. Lee, C. M. Lieber, Synthesis of monolithic graphene–graphite integrated electronics. *Nat. Mater.* **11**, 120–125 (2012).

31. M.-S. Lee, K. Lee, S.-Y. Kim, H. Lee, J. Park, K.-H. Choi, H.-K. Kim, D.-G. Kim, D.-Y. Lee, S. Nam, J.-U. Park, High-performance, transparent, and stretchable electrodes using graphene–metal nanowire hybrid structures. *Nano Lett.* **13**, 2814–2821 (2013).

32. M.-S. Lee, J. Kim, J. Park, J.-U. Park, Studies on the mechanical stretchability of transparent conductive film based on graphene-metal nanowire structures. *Nanoscale Res. Lett.* **10**, 27 (2015).

33. J. Mujal, E. Ramon, E. Díaz, J. Carrabina, Á. Calleja, R. Martínez, L. Terés, Inkjet printed antennas for NFC systems, in *Proceedings of the 2010 17th IEEE International Conference on Electronics, Circuits and Systems*, Athens, Greece, 12 to 15 December 2010.

34. J. Kim, M.-S. Lee, S. Jeon, M. Kim, S. Kim, K. Kim, F. Bien, S. Y. Hong, J.-U. Park, Highly transparent and stretchable field-effect transistor sensors using graphene–nanowire hybrid nanostructures. *Adv. Mater.* **27**, 3292–3297 (2015).

35. C. Joossen, E. Lanckacker, N. Zakaria, C. Koppen, J. Joossens, N. Cools, I. De Meester, A.-M. Lambeir, P. Delputte, L. Maes, P. Cos, Optimization and validation of an existing, surgical and robust dry eye rat model for the evaluation of therapeutic compounds. *Exp. Eye Res.* **146**, 172–178 (2016).

36. J. Kim, J. Kim, M. Ku, E. Cha, S. Ju, W. Y. Park, K. H. Kim, D. W. Kim, P.-O. Berggren, J.-U. Park, Intraocular pressure monitoring following islet transplantation to the anterior chamber of the eye. *Nano Lett.* **20**, 1517–1525 (2020).

37. Y.-G. Park, H. S. An, J.-Y. Kim, J.-U. Park, High-resolution, reconfigurable printing of liquid metals with three-dimensional structures. *Sci. Adv.* **5**, eaaw2844 (2019).

38. Y.-G. Park, H. Min, H. Kim, A. Zhexembekova, C. Y. Lee, J.-U. Park, Three-dimensional, high-resolution printing of carbon nanotube/liquid metal composites with mechanical and electrical reinforcement. *Nano Lett.* **19**, 4866–4872 (2019).

39. Q. Yang, Y. Zhang, X. Liu, N. Wang, Z. Song, K. Wu, A comparison of the effects of benzalkonium chloride on ocular surfaces between C57BL/6 and BALB/c mice. *Int. J. Mol. Sci.* **18**, 509 (2017).

40. American Society for Testing Materials, Standard Guide for Accelerated Aging of Sterile Barrier Systems for Medical Devices. ASTM F1980-07 (2011).

41. R. Sambursky, Presence or absence of ocular surface inflammation directs clinical and therapeutic management of dry eye. *Clin. Ophthalmol.* **10**, 2337–2343 (2016).

42. D. H. Keum, S.-K. Kim, J. Koo, G.-H. Lee, C. Jeon, J. W. Mok, B. H. Mun, K. J. Lee, E. Kamrani, C.-K. Joo, S. Shin, J.-Y. Sim, D. Myung, S. H. Yun, Z. Bao, S. K. Hahn, Wireless smart contact lens for diabetic diagnosis and therapy. *Sci. Adv.* **6**, eaba3252 (2020).

43. Y.-R. Lin, C.-C. Hung, H.-Y. Chiu, P.-H. Chang, B.-R. Li, S.-J. Cheng, J.-W. Yang, S.-F. Lin, G.-Y. Chen, Noninvasive glucose monitoring with a contact lens and smartphone. *Sensors* **18**, 3208 (2018).

44. M. Ku, J. Kim, J.-E. Won, W. Kang, Y.-G. Park, J. Park, J.-H. Lee, J. Cheon, H. H. Lee, J.-U. Park, Smart, soft contact lens for wireless immunosensing of cortisol. *Sci. Adv.* **6**, eabb2891 (2020).

45. J. V. Greiner, A single LipiFlow® Thermal Pulsation System treatment improves meibomian gland function and reduces dry eye symptoms for 9 months. *Curr. Eye Res.* **37**, 272–278 (2012).

46. D. Badawi, TearCare® system extension study: Evaluation of the safety, effectiveness, and durability through 12 months of a second TearCare® treatment on subjects with dry eye disease. *Clin. Ophthalmol.* **13**, 189–198 (2019).

47. M. T. M. Wang, J. Feng, J. Wong, P. R. Turnbull, J. P. Craig, Randomised trial of the clinical utility of an eyelid massage device for the management of meibomian gland dysfunction. *Cont. Lens Anterior Eye* **42**, 620–624 (2019).

Citation: J. Jang, J. Kim, H. Shin, Y.-G. Park, B. J. Joo, H. Seo, J.-e. Won, D. W. Kim, C. Y. Lee, H. K. Kim, J.-U. Park, Smart contact lens and transparent heat patch for remote monitoring and therapy of chronic ocular surface inflammation using mobiles. *Sci. Adv.* **7**, eabf7194 (2021).